Materials Advances

ROYAL SOCIETY OF CHEMISTRY

PAPER

View Article Online
View Journal | View Issue

Cite this: *Mater. Adv.*, 2025, 6, 409

Unravelling the oxygen exchange mechanism on $La_2Ce_2O_7$†

Yizhou Shen, Vincent Thoréton and Reidar Haugsrud*

Received 21st August 2024,
Accepted 2nd December 2024

DOI: 10.1039/d4ma00840e

rsc.li/materials-advances

Understanding the mechanism of the oxygen exchange rate between the gas-phase and the oxide surface is essential to utilize electrochemical transport of oxygen in ceria-based materials for sustainable technologies. This contribution applies pulse isotope exchange (PIE) to investigate the oxygen exchange mechanism on $La_2Ce_2O_7$ and 5% Pr-substituted $La_2Ce_2O_7$. The oxygen exchange kinetics is rate-limited by the dissociation of adsorbed molecular oxygen. Pr substitution increases the surface kinetics, presumably due to an increased concentration of electronic defects that enhances charge transfer of electronic defects at the surface. Humidity decreases the exchange rate due to the selective dissociative adsorption of water molecules into surface oxygen vacancies, forming hydroxide defects. This effect diminishes with increasing temperature due to the exothermic nature of hydration.

1. Introduction

The exchange of oxygen between the gas-phase and the oxide surface, as well as the transport of oxide ions and electrons in the bulk of the oxide, are mutually important for the performance of solid oxide fuel and electrolyzer cells (SOFC and SOEC), interconverting chemical and electrical energy.[1–4] Nevertheless, which functional properties of oxides promote the oxygen reduction reaction (ORR) and why, remain subjects of debate.

Rare-earth (RE) substituted ceria, $Ce_{1-x}RE_xO_{2-\delta}$, is among the best oxide ion conductors, and the partial reducibility of Ce(IV) yields electronic defects, jointly giving rise to various functional properties.[5] Moreover, these materials are ideal for fundamental studies and have been central in developing the understanding of oxygen exchange mechanisms.[6–25] Substitution with multivalent RE cations (>5 atomic%) introduces impurity electron bands, further facilitating ionization of adsorbed oxygen species at the surface, increasing the oxygen exchange rate, $\Re_0$, by orders of magnitude.[21,26–30] In several ceria-based materials, the apparent activation energy of $\Re_0$ has been reported to be significantly higher at high temperatures (above 700 to 800 °C) compared to lower temperatures (E_a > 2 eV *vs.* E_a < 1.5 eV, respectively).[23,31–33] In this respect, it has been speculated whether the omnipresent water vapor influences the oxygen exchange mechanism in the low-temperature range.[33]

Although debated, the crystal structure of $La_2Ce_2O_7$ has been reported as a disordered fluorite structure, closely related to pristine ceria,[34–37] and can consequently be regarded as 50% La-substituted CeO_2, *i.e.*, $Ce_{0.5}La_{0.5}O_{\sim 1.75}$. Unlike ceria, the material exhibits predominantly ionic conductivity even at low oxygen partial pressures (*e.g.*, $<10^{-20}$ atm at 700 °C[38,39]). Its ionic conductivity at 600 °C is approximately one order of magnitude lower than GDC, but only a factor of three lower than YSZ.[38–40] $La_2Ce_2O_7$ dissolves hydroxide defects up to high temperatures (~800 °C) and demonstrates appreciable proton conductivity under humidified conditions.[39,41–44] Thus, $La_2Ce_2O_7$ exhibits conductivity characteristics interesting for diverse applications.[45–47]

There are a few studies on the oxygen exchange kinetics of ceria with La (≪50%) and co-doped with Pr.[48–50] La substitution increases the oxygen exchange coefficient, k_s (relation to $\Re_0$ shown in the ESI†), of Pr-doped ceria and its apparent activation energy.[50] It has been speculated that this behavior indicates a change in the point defects controlling the rate-determining process, *e.g.*, shifting from oxygen vacancies to electronic defects.[50,51]

Oxygen vacancies and electronic defects play crucial roles in the fundamental processes involved in oxygen exchange, and material properties that affect the concentration of these defects are essential.[21,52] Recently, the interaction between the electronic band structure at the surface and adsorbed oxygen species has been emphasized. Electron transfer from the surface to adsorbed oxygen species is facilitated by the reduction of the material's band gap, which, in the case of Pr-substituted ceria, is attributed to the generation of a Pr impurity band within the band gap.[27–30,50]

The materials being studied here, $La_2Ce_2O_7$ (LaC) and 5% Pr-substituted $La_2Ce_2O_7$, $La_2Ce_{1.95}Pr_{0.05}O_{7-\delta}$ (5PrLaC) represent

Department of Chemistry, Centre for Materials Science and Nanotechnology, University of Oslo, Gaustadalléen 21, NO-0349 Oslo, Norway

† Electronic supplementary information (ESI) available. See DOI: https://doi.org/10.1039/d4ma00840e

extremes of oxygen-deficient, ceria-like disordered fluorite structures, substituting 50% of Ce(IV) with the more basic La(III). Additionally, Pr substitution may promote the formation of electronic defects through Pr(III)–Pr(IV) redox transitions. Accordingly, these materials serve as suitable model systems to investigate the individual effects of these parameters on oxygen exchange kinetics. Moreover, the significant bulk concentration and conductivity of protons in lanthanum cerates in the presence of water vapor, even at temperatures above 700 °C (approximately 1 mol% at 700 °C in 0.025 atm H_2O), make these materials particularly interesting for studying the effects of water vapor on oxygen exchange kinetics.[39,44]

On these bases, we investigated the oxygen exchange mechanism and potential effects of water vapor on the exchange rate of $La_2Ce_2O_7$-based materials utilizing pulse isotope exchange (PIE) measurements. Building on our experimental findings and a further discussion of the literature data for ceria-based materials, we address the understanding of the oxygen exchange properties of this technologically important class of materials.

2. Gas-phase isotope studies

Oxygen exchange between the gas-phase and the oxide surface involves a series of elementary steps. Initially, gas-phase transport occurs towards the surface, followed by oxygen adsorption and potential dissociation into various adsorbed species. Additional steps required for oxygen exchange include the transfer of electrons to the adsorbed oxygen species, surface diffusion, and incorporation of oxide ions. These steps may all limit the overall rate of oxygen exchange.

The exchange reaction at the oxide surface can be described by Kröger–Vink notation as:[53]

$$O_2(g) + 2v_O^{\bullet\bullet} \overset{\Re_0}{\longleftrightarrow} 2O_O^{\times} + 4h^{\bullet} \quad (1)$$

where $v_O^{\bullet\bullet}$ represents oxygen vacancies, $O_O^{\times}$ lattice oxide ions and $h^{\bullet}$ electron holes. At equilibrium, the reaction rates of oxygen entering and leaving the surface are equal and characterized by $\Re_0$ (in mol O m^{-2} s^{-1}), *i.e.*, the equilibrium oxygen exchange rate.

Several techniques have been developed to investigate the oxygen exchange kinetics, including electrical conductivity relaxation (ECR),[54,55] isotope exchange followed by depth profiling (IEDP) with secondary ion mass spectrometry (SIMS)[56,57] and gas phase analysis methodologies (GPA).[58,59] ECR measurements provide information on chemical diffusion and surface exchange coefficients, while IEDP with SIMS gives insight into the oxygen tracer surface exchange and diffusion coefficients. GPA, on the other hand, involves continuous monitoring of isotopologue transients in a labeled atmosphere surrounding the oxides in chemical equilibrium with the reaction conditions. Under the steady-state approximation, $\Re_0$ can principally be broken down into the rates of dissociative adsorption, $\Re_{dis}$, and incorporation, $\Re_{inc}$, providing further insight into the underlying exchange mechanism.[60,61]

During PIE measurements, powder samples are pre-equilibrated at the chosen oxygen partial pressure, p_{O_2}, and temperature in a packed-bed quartz reactor under a constant laminar gas flow. An ^{18}O enriched pulse with the same p_{O_2} as during pre-annealing is introduced upstream through the powder bed for oxygen exchange. The fractions of ^{16}O and ^{18}O (f_g^{16} and f_g^{18}) are determined from the concentrations of the diatomic isotopologues $^{16}O_2$, $^{16}O^{18}O$ and $^{18}O_2$ (f_g^{32}, f_g^{34} and f_g^{36}) at the reactor outlet by means of a quadrupole mass spectrometer (Pfeiffer QME Prisma 220). Provided there is chemical equilibrium between the gas-phase and the oxide and that the requirements of the PIE model are fulfilled,[60] the simultaneous decrease in f_g^{36} along with the increase in f_g^{34} and f_g^{32} reflects the scrambling of ^{16}O and ^{18}O as a consequence of dissociation and incorporation (in addition to recombination and desorption) of chemisorbed surface oxygen species into the oxide lattice. The requirement for chemical equilibrium should be recognized in relation to the kinetic parameters derived from gas-phase isotope analysis methods, as these parameters represent balanced exchange rate coefficients.

To investigate the effects of water vapor on the exchange rate, the powder was equilibrated in carrier gas mixtures containing 3% H_2O. However, the labeled oxygen pulse used for the exchange experiments was bottle-dry. In this way, the humidity present during the oxygen exchange is determined by the amount of adsorbed hydroxide defects on the surface of the powder. The amount of adsorbed hydroxide defects on the powder surface varies with temperature, following the thermodynamics of the interactions between water and the oxide surface. These interactions involve the chemisorption of water molecules, potential dissociation, and incorporation of these species to form hydroxide defects. We emphasize that the influence of water encountered herein is solely qualitative in nature. It serves as a basis for further discussion and analysis. To gain comprehensive understanding of these interactions and their effects on the oxygen exchange rate, additional quantitative studies are necessary.

3. Experimental

LaC was synthesized *via* solid-state synthesis. Stoichiometric amounts of cerium(IV) oxide nanopowders (particle size <50 nm, 99.95% purity; Sigma-Aldrich) and lanthanum(III) oxide (≥99.9% purity; Sigma-Aldrich), pre-dried at 900 °C, were dispersed in isopropanol and mixed in a roller mill (Model 12VS, Capco) for 24 hours.

The resulting suspension was dried and then calcined at 1000 °C for 3 hours. The powders were shaped into pellets through uniaxial pressing, followed by sintering at 1580 °C in air for 4 hours, with heating and cooling rates of 3 °C min^{-1}, giving a relative density of >94% (determined by Archimedes' method). Finally, the dense pellets were crushed and sieved into three fractions with particle sizes: 90–125 μm, 40–60 μm, and <20 μm. We assume that the agglomerates maintain the relative density of the sintered pellets before crushing.

5PrLaC was synthesized according to a Pechini-based route. Stoichiometric amounts of lanthanum(III) nitrate hexahydrate

(≥99.9%; Sigma-Aldrich) and praseodymium nitrate hexahydrate (99.9%; Sigma-Aldrich) were dissolved in deionized water, followed by mixing with citric acid (99%; Sigma-Aldrich) under continuous stirring at 80 °C. The molar ratio between the cations and citric acid was 1 : 2.

After evaporating the water, the precursor was further annealed at 250 °C, resulting in a xerogel, which was calcined at 1000 °C for 3 hours in air. Sintering at 1580 °C in air yielded a relative density of 93%, and the fractioning procedures were the same as for LaC.

X-ray diffraction (XRD) and scanning electron microscopy (SEM) images of the powder products are presented in the ESI.†

The PIE procedure was conducted following the method described by Bouwmeester *et al.*,[60,62] with the detailed procedure outlined in the ESI.† The temperature range used to extract kinetic parameters was from 650 to 950 °C, which is significantly lower than the sintering temperature. The temperature range measured varied slightly depending on the materials and gas composition. The temperature at which the interaction between oxygen in the gas-phase and the surface becomes detectable with the quadrupole mass spectrometer (QMS) is referred to as the onset temperature, T_{onset} (°C).

The p_{O_2} range was between 0.005 and 0.21 atm for both dry and wet carrier gases. The water vapor pressure p_{H_2O} (0.03 atm) in the wet carrier gas was determined by the temperature of the water reservoir through which the carrier gas flowed before entering the reactor. One should note that to enable accurate measurements at the lowest p_{O_2}, 99% ^{18}O gas was used as the source for the isotope mixtures, different from the more conventional isotope enrichment of >97% ^{18}O for the higher p_{O_2}.

The PIE measurements were conducted in the surface-controlled regime. This was verified through separate gas-phase isothermal isotope exchange (IIE) experiments, which showed that the average particle sizes were considerably smaller than the characteristic length, l, where $l = D/k_s$ (D is the bulk self-diffusion coefficient). Accordingly, it was assumed that there is no concentration gradient of oxygen isotopes in the oxide bulk, *i.e.*, bulk diffusion has virtually no effect on the measurements of oxygen surface exchange.

4. Results

Fig. 1 and 2 depict representative examples of the evolution of the pulse response in PIE as a function of temperature for LaC and 5PrLaC in bottle-dry and wet (0.03 atm H_2O) carrier gases at 0.02 atm O_2. The fraction of $^{36}O_2$, f_g^{36}, gradually decreases above 500–600 °C (T_{onset}) because of the scrambling of adsorbed ^{16}O and ^{18}O at the surface and the incorporation of ^{18}O into the bulk of the oxide. T_{onset} is lower for the doped compared to the undoped material.

The presence of water vapor slightly increases T_{onset} and alters the profile shape accordingly. It is worth noting that the increased formation of $^{16}O^{18}O$ qualitatively indicates slower incorporation relative to dissociative adsorption and associative desorption.

Fig. 3 presents the oxygen partial pressure dependence of $\Re_0$ for both bottle-dry and humidified conditions for (a) LaC and (b) 5PrLaC, including the p_{O_2} dependences obtained from linear fitting of the data according to double logarithmic representations. Fig. 4 displays the isobaric temperature dependence of $\Re_0$ corresponding to the exchange rates in Fig. 3 for the lowest and highest measured p_{O_2}. Generally, there is some scatter in the data with respect to functional dependences, especially for LaC. Nevertheless, one may conclude from Fig. 3 and 4 that the overall exchange rate is slightly higher for the Pr-substituted material and, moreover, that the rate generally decreases and becomes more activated under humidified conditions.

The oxygen partial pressure dependence for 5PrLaC is relatively consistent, varying in the range $\Re_0 \propto {p_{O_2}}^{0.65\text{ to }0.75}$. For LaC, the data points for the three highest oxygen partial pressures follow an essentially $\Re_0 \propto {p_{O_2}}^{0.37\text{ to }0.5}$ dependence, whereas the data at 0.005 atm O_2 deviate and are lower than expected according to the functional dependence from higher p_{O_2}. With the present scatter, there is no distinct difference between the p_{O_2} dependences in both bottle-dry and humidified conditions for the two materials.

For the temperature dependence of $\Re_0$ in Fig. 4: firstly, the apparent activation energy decreases when going from undoped to 5% Pr-doped $La_2Ce_2O_7$. Secondly, the data at 0.005 atm O_2 for LaC, which deviate from the ''linear'' dependence at higher

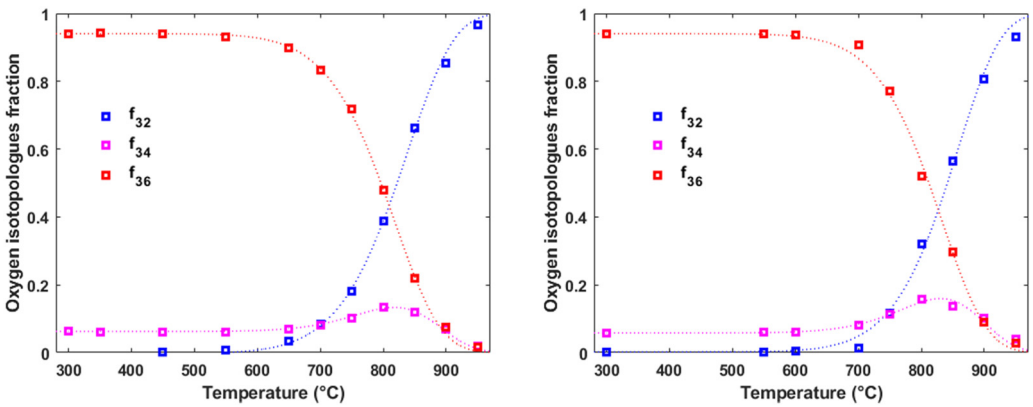

Fig. 1 Oxygen isotopologue fractions as a function of temperature for $La_2Ce_2O_7$ at p_{O_2} = 0.02 atm in dry carrier gas (on the left) and wet carrier gas (on the right), respectively. In both cases, dry pulses were employed. The dotted lines represent the fits to the models (see ESI,† Section S1 and eqn (S17), (S22)–(S24)). The constant level of $^{16}O^{18}O$ up to T_{onset} is due to the purity of the isotope-labeled gas (97% ^{18}O), reflecting the distribution of the isotopologues.

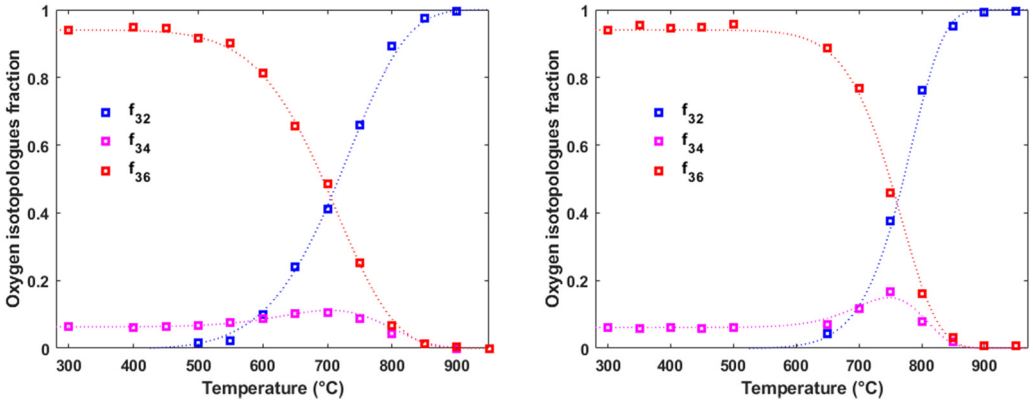

Fig. 2 Oxygen isotopologue fractions as a function of temperature for $La_2Ce_{1.95}Pr_{0.05}O_{7-\delta}$ at p_{O_2} = 0.02 atm in dry carrier gas (on the left) and wet carrier gas (on the right), respectively. In both cases, dry pulses were employed. The dotted lines represent the fits to the models (see ESI,† Section S1 and eqn (S17), (S22)–(S24)).

p_{O_2}, exhibit lower apparent activation energies than those at higher oxygen partial pressures. Finally, the apparent activation energy measured across the temperature range increases going from bottle-dry to humidified conditions, and particularly so for the Pr-doped material. This is emphasized in Fig. 5, which presents the temperature dependence of $\Re_0$ at 0.02 atm O_2. Notably, the wet data deviate from linear Arrhenius behavior, as the difference in $\Re_0$ between wet and dry carrier gases gradually diminishes with increasing temperature. For 5PrLaC, the apparent activation energy decreases from approximately 190 to 130 kJ mol^{-1}, whereas it remains essentially constant for LaC ($\sim$150 kJ mol^{-1}).

5. Discussion

Preliminary understanding of the oxygen exchange mechanism may be obtained by visually analyzing the development of the oxygen isotopologues in the PIE profiles (*cf.* Fig. 1 and 2). Low f_{34} levels indicate that the scrambling of dissociated oxygen species adsorbed on the surface is sluggish relative to the incorporation of these surface species. In other words, one of the elementary reactions involved in oxygen dissociation limits the overall oxygen exchange.

More quantitative approaches involve addressing the p_{O_2} dependence of $\Re_0$ using chemical kinetics, as different sequences of elementary reactions lead to different dependences on the oxygen partial pressure.[63,64] For the Pr-doped material, Fig. 3 shows that $\Re_0 \propto {p_{O_2}}^m$, $m \in [0.5\text{–}1]$, supporting that the rate-determining step (rds) involves the dissociation of molecular oxygen.[21] The behavior of the undoped material is less conclusive due to more scattered data, and even more so, whether or not the data points at 0.005 atm of oxygen are included. Leaving the 0.005 atm dataset out, the oxygen partial pressure dependences are consistently lower ($\Re_0 \propto {p_{O_2}}^m$, $m \in [0.37\text{–}0.49]$) for LaC compared to the Pr-substituted material, indicating differences in the overall oxygen exchange mechanism.

Although the $^{36}O_2$ pulse is dry, there are distinct differences between the detailed effects of reaction conditions on the exchange rates for bottle-dry and wet carrier gases (*cf.* Fig. 1–5).

Considering commonly applied reaction mechanisms for oxygen exchange on similar ceria-based materials, the adsorption of gaseous oxygen molecules with the transfer of one electronic defect can be denoted as:[63,65–67]

$$O_{2,g} + {}^{*} \leftrightarrow O_{2,ad} \quad (2)$$

$$O_{2,ad} \leftrightarrow {O_{2,ad}}^{-} + h^{\bullet} \quad (3)$$

Whether electrons or electron holes are involved in the elementary reactions other than the rate-determining step does not alter the oxygen partial pressure dependence of the overall exchange rate since these reactions are at quasi equilibrium.[63,68–71] For dissociative adsorption, one may differentiate between mechanisms mediated by oxygen vacancies (4-a) and (5-a) and those that are not (4-b) and (5-b):

$$O^{-}_{2,ad} + v^{\bullet\bullet}_{O} \underset{k^{-}_{dis.a}}{\overset{k_{dis.a}}{\longleftrightarrow}} O^{-}_{ad} + O^{\times}_{O} + 2h^{\bullet} \quad (4\text{-a})$$

$$O^{-}_{2,ad} + * \underset{k^{-}_{dis.b}}{\overset{k_{dis.b}}{\longleftrightarrow}} 2O^{-}_{ad} + h^{\bullet} \quad (4\text{-b})$$

$$O^{-}_{2,ad} + v^{\bullet\bullet}_{O} + 2e' \underset{k^{-}_{dis.a}}{\overset{k_{dis.a}}{\longleftrightarrow}} O^{-}_{ad} + O^{\times}_{O} \quad (5\text{-a})$$

$$O^{-}_{2,ad} + e' + * \underset{k^{-}_{dis.b}}{\overset{k_{dis.b}}{\longleftrightarrow}} 2O^{-}_{ad} \quad (5\text{-b})$$

The reactions are outlined both with electrons from the valence band (formation of holes) and the conduction band in the reactions in eqn (4) and (5), respectively. The adsorbed peroxide species formed during dissociation are incorporated along with the transfer of another electronic defect:

$$O^{-}_{ad} + v^{\bullet\bullet}_{O} \underset{k^{-}_{inc}}{\overset{k_{inc}}{\longleftrightarrow}} O^{\times}_{O} + h^{\bullet} \quad (6)$$

For the reactions in eqn (2)–(6), * denotes adsorption sites different from $v^{\bullet\bullet}_{O}$. $O_{2,g}$ and $O_{2,ad}$ represent neutral diatomic oxygen species in the gas-phase and adsorbed on the surface, respectively. $O^{-}_{2,ad}$ and O^{-}_{ad} refer to charged, adsorbed oxygen species, *i.e.*, a superoxide and a peroxide species, respectively.

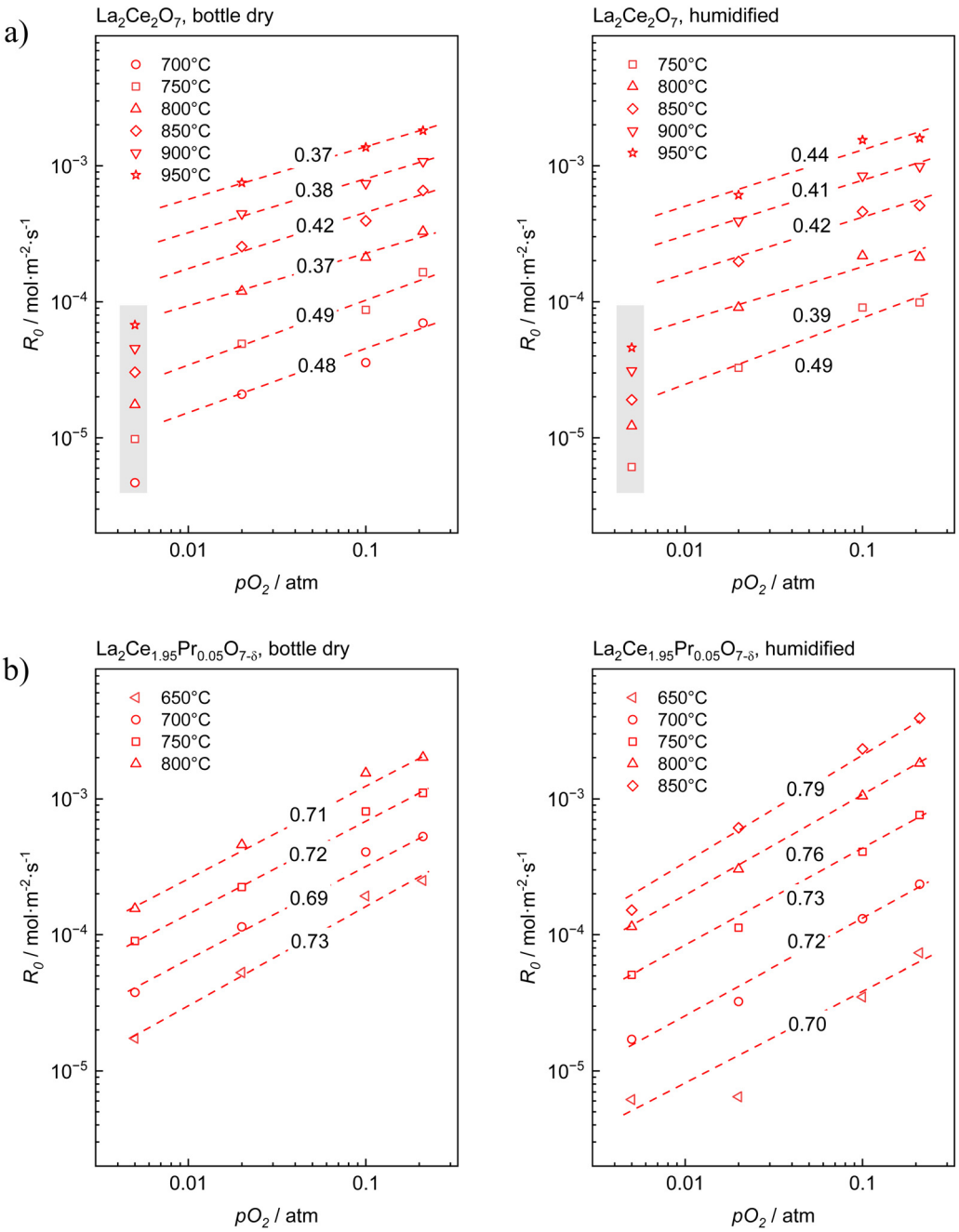

Fig. 3 Overall oxygen exchange rate, $\Re_0$, as a function of the oxygen partial pressure, p_{O_2}, for (a) $La_2Ce_2O_{7-\delta}$ and (b) $La_2Ce_{1.95}Pr_{0.05}O_{7-\delta}$ with dry and wet carrier gases. The dashed lines represent least-squares fitting of the data according to $\Re_0 \propto {p_{O_2}}^m$ and the respective slopes, m, are included. Notably, all graphs exhibit the same ranges on the axes to facilitate comparison.

For the scheme facilitated by oxygen vacancies, one oxygen species incorporates directly as part of the dissociation. The leftover adsorbed peroxide species formed in the reactions can either be incorporated through the consecutive reaction in eqn (6) or recombine with another adsorbed species and desorb as an oxygen molecule. Despite potential recombination and desorption, oxygen exchange is completed by the direct incorporation of the oxygen species into the oxygen vacancy. Since the incorporation of oxygen takes place simultaneously with dissociation in both eqn (4-a) and (5-a) *via* oxygen vacancies, parallel to the incorporation in eqn (6), this has been denoted as a parallel-like mechanism in the literature.[61,72] The reactions in (4-b) and (5-b) exclusively represent dissociation and must be followed by the incorporation reaction (eqn (6)) to complete the exchange between gas-phase oxygen and oxide ions in the surface sublattice. Accordingly, these reactions imply a serial scheme.[72,73]

Bouwmeester *et al.*[60,61] have demonstrated that $\Re_0$ can be deconvoluted into individual pairs of $\Re_{dis}$ and $\Re_{inc}$ from the time dependence of the fractions of oxygen isotopes and

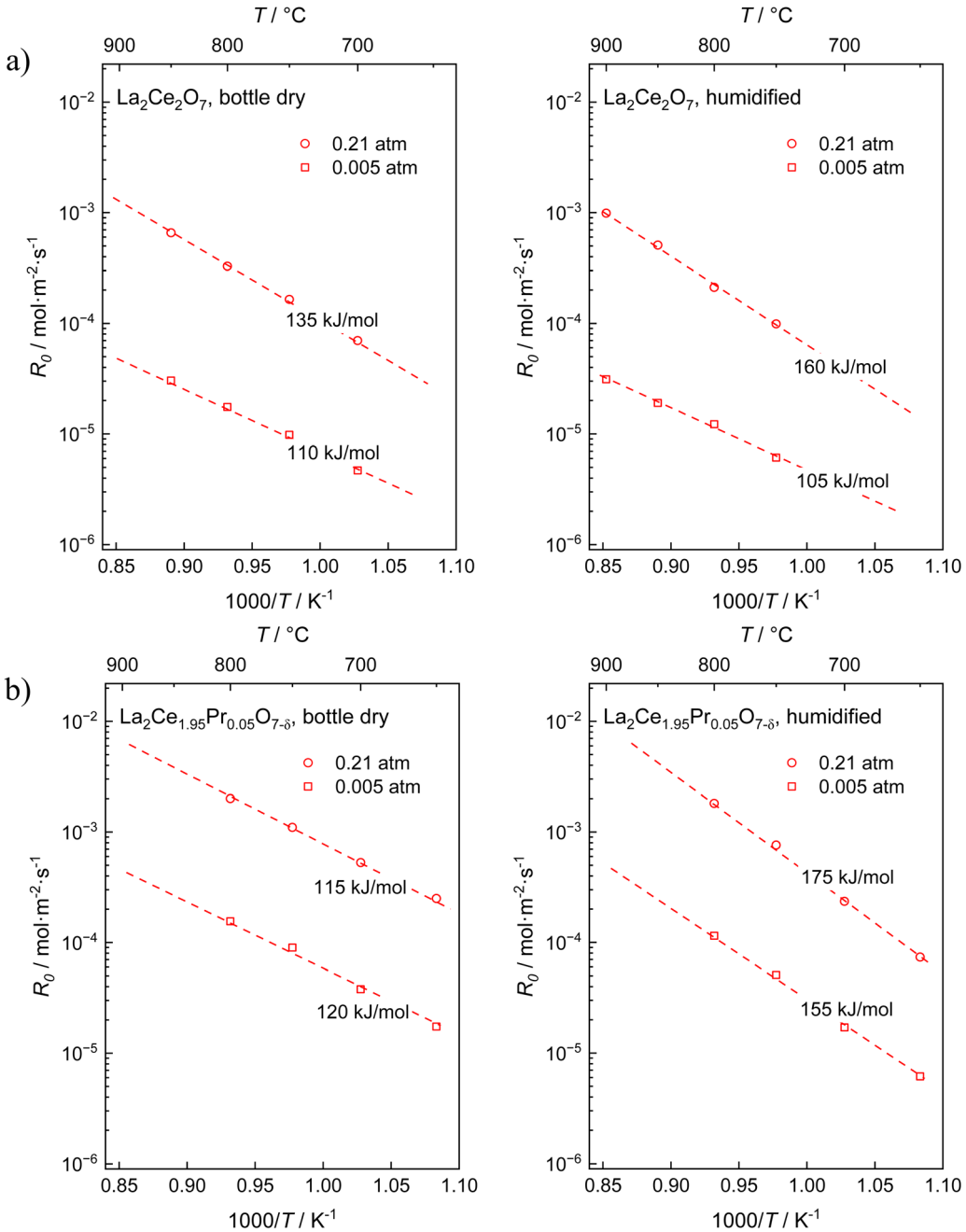

Fig. 4 Overall oxygen exchange rate, $\Re_0$, as a function of the inverse absolute temperature for the highest and lowest p_{O_2} for (a) $La_2Ce_2O_{7-\delta}$ and (b) $La_2Ce_{1.95}Pr_{0.05}O_{7-\delta}$ with dry and wet carrier gases. The dashed lines represent least-squares fitting of the data according to Arrhenius behavior, including the apparent activation energies. All graphs exhibit the same ranges on the axes to facilitate comparison.

isotopologues in the pulse response. The relationship between these rate constants differs for the parallel (eqn (7), with p in superscript for parallel) and serial mechanism (eqn (8), with s in superscript for serial):

$$\Re_0 = \frac{1}{2}\Re^{p}_{dis}\left(1 + \frac{\Re^{p}_{inc}}{\frac{1}{2}\Re^{p}_{dis} + \Re^{p}_{inc}}\right) \quad (7)$$

$$\frac{1}{\Re_0} = \frac{1}{\Re^{s}_{dis}} + \frac{1}{\Re^{s}_{inc}} \quad (8)$$

(Eqn (7) and (8) were derived in the literature[61,72] and the derivation is also presented in the ESI,† for completeness). It is important to acknowledge the uncertainty associated with the deconvoluted rate constants, especially for the rapid incorporation rate when the formation of $^{16}O^{18}O$ is low. Nevertheless, the two pairs of $\Re_{dis}$ and $\Re_{inc}$, along with their dependence

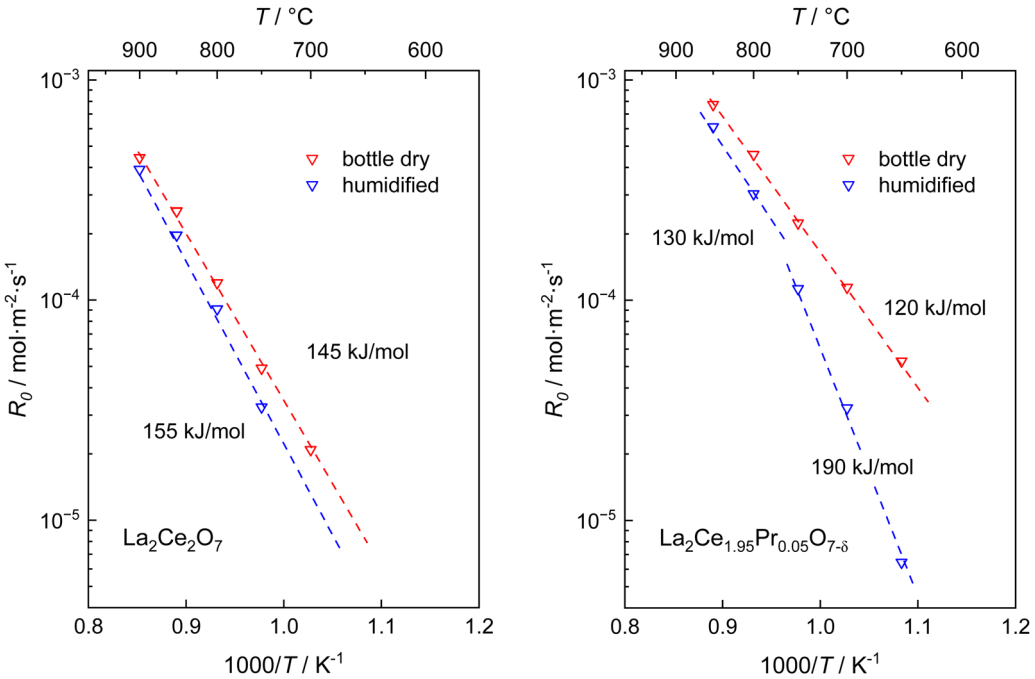

Fig. 5 Temperature dependence of the overall oxygen surface exchange rates of $La_2Ce_2O_7$ and $La_2Ce_{1.95}Pr_{0.05}O_{7-\delta}$ at p_{O_2} = 0.02 atm in dry and wet carrier gases. In both cases, dry pulses were employed.

on the reaction conditions, may offer additional clarification and further insight into the oxygen exchange mechanism.

The relative influence of dissociation and incorporation can be illustrated using contour plots, as introduced by den Otter *et al.*[72] Fig. 6 displays a contour plot of the ratios between $\Re_0$ and $\Re_{dis}$, corresponding to the fraction of the oxygen incorporated (exchanged between the gas-phase and surface) relative to that dissociatively adsorbed according to the serial and parallel models, respectively. 5PrLaC shows a higher fraction of incorporation relative to dissociation than for LaC. Additionally, the presence of water vapor decreases the relative rate of incorporation for both materials.

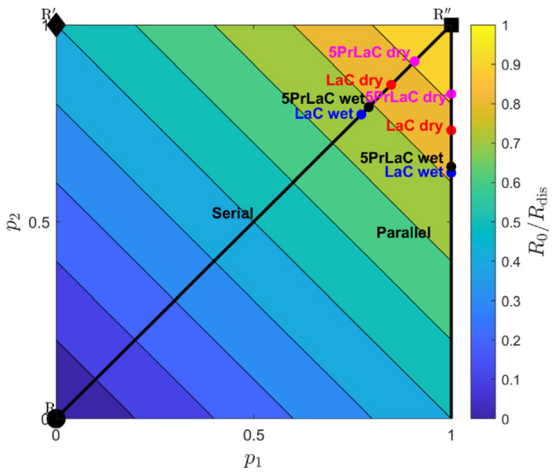

Fig. 6 Contour plot of the ratio of the overall oxygen exchange rate (hetero exchange rate) to the dissociative adsorption rate at 750 °C and 0.02 atm of O_2. p_1 and p_2 are the independent probabilities of each oxygen atom in a dissociated oxygen molecule being incorporated into the oxide. Further derivation and interpretation of the contour plot can be found in the ESI.†[72,74,75]

As shown in Fig. 7 and 8, the temperature and oxygen partial pressure dependences of the rate constants are deconvoluted according to eqn (7) and (8), corresponding to the parallel and serial mechanisms, respectively. The pairs of rate constants exhibit rather similar functional behavior, but their relative contributions to the overall exchange rate vary. For the serial mechanism, the incorporation is generally faster than dissociative adsorption, whereas for the parallel mechanism, the rates are more similar.

The temperature dependences for the dissociation and incorporation display some notable trends. Firstly, the exchange rates are higher for the doped material. Secondly, the apparent activation energy is higher under humidified compared to bottle-dry conditions (*cf.* Fig. 5). This is most significant for the Pr-substituted material and is also more pronounced for incorporation than for dissociative adsorption. Under bottle-dry conditions, the activation energy for the dissociative adsorption is, generally, higher for LaC compared to for 5PrLaC, a trend that reverses under humidified conditions.

Examples of p_{O_2} dependence on the rate constants are shown in Fig. 8. Overall, the oxygen partial pressure dependence is relatively consistent and corresponds to the behavior expected for dissociative adsorption and incorporation (see also ESI,† Fig. 6 and 7). The dissociation rates largely reflect $\Re_0$, but with slightly stronger oxygen partial pressure dependences. The individual behavior manifests the differences in the exchange mechanism between the pristine and doped material,

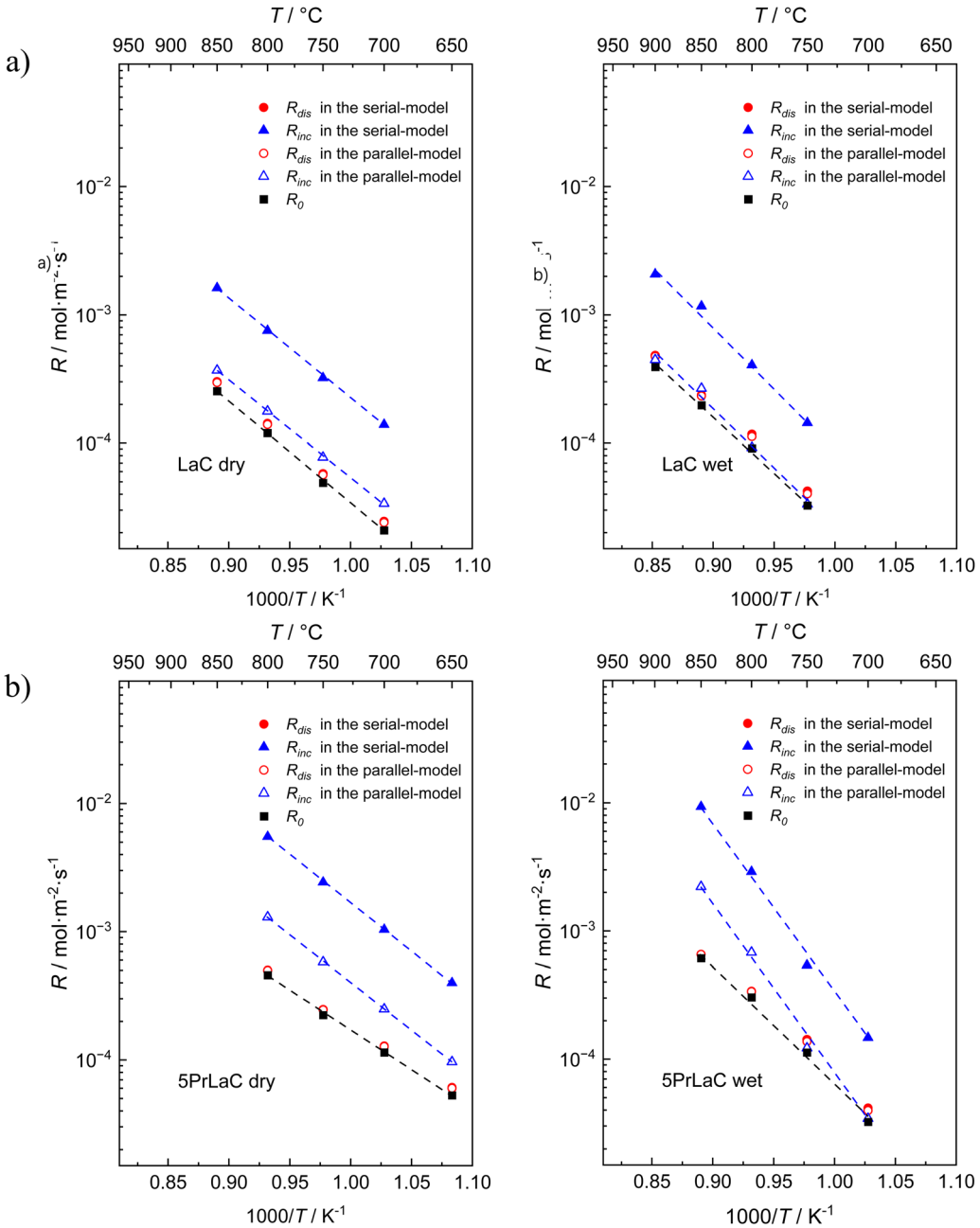

Fig. 7 Temperature dependence of the deconvoluted oxygen surface exchange rates in dry and wet carrier gases at p_{O_2} = 0.02 atm, for (a) $La_2Ce_2O_7$ and (b) $La_2Ce_{1.95}Pr_{0.05}O_7$. The entire dataset is presented in the Section S5 (ESI†).

$\Re_{dis} \propto {p_{O_2}}^{0.47-0.7}$ and $\Re_{dis} \propto {p_{O_2}}^{0.75-0.97}$, respectively. The p_{O_2} dependence of $\Re_{inc}$ is scattered but generally decreases with increasing temperature in the range $m \in [0, 0.05]$, becoming essentially invariant at the higher temperatures $\left(\Re_{inc} \propto p^0_{O_2}\right)$.

Generally, dissociative adsorption governs the oxygen exchange for the serial mechanism, as $\Re^s_{dis}$ is significantly lower than $\Re^s_{inc}$. Since these values are more similar when deconvoluting of $\Re_0$ according to the parallel-like mechanism, and the incorporation rate is independent of p_{O_2}, $\Re^p_{dis}$ eventually surpasses $\Re^s_{inc}$. In other words, reaction (4-a) or (5-a) contributes relatively more than reaction (6) to the overall oxygen incorporation at the highest oxygen partial pressures. Since incorporation is realized as part of the dissociation, oxygen exchange is maintained.

The defect structure of the surface influences the temperature and p_{O_2} dependences of the exchange rate. However, since these surface properties are rarely known, one has to rely on the properties of bulk and evaluate potential deviations from it based on developed theories for space charge layers. Merkle, Maier and coworkers[21,76] have discussed potential differences in the defect chemistry between the bulk and the surface, including ceria-based materials, relevant to the present investigation. Based on their findings and other literature reporting negligible surface charges for ceria-based materials, as well as

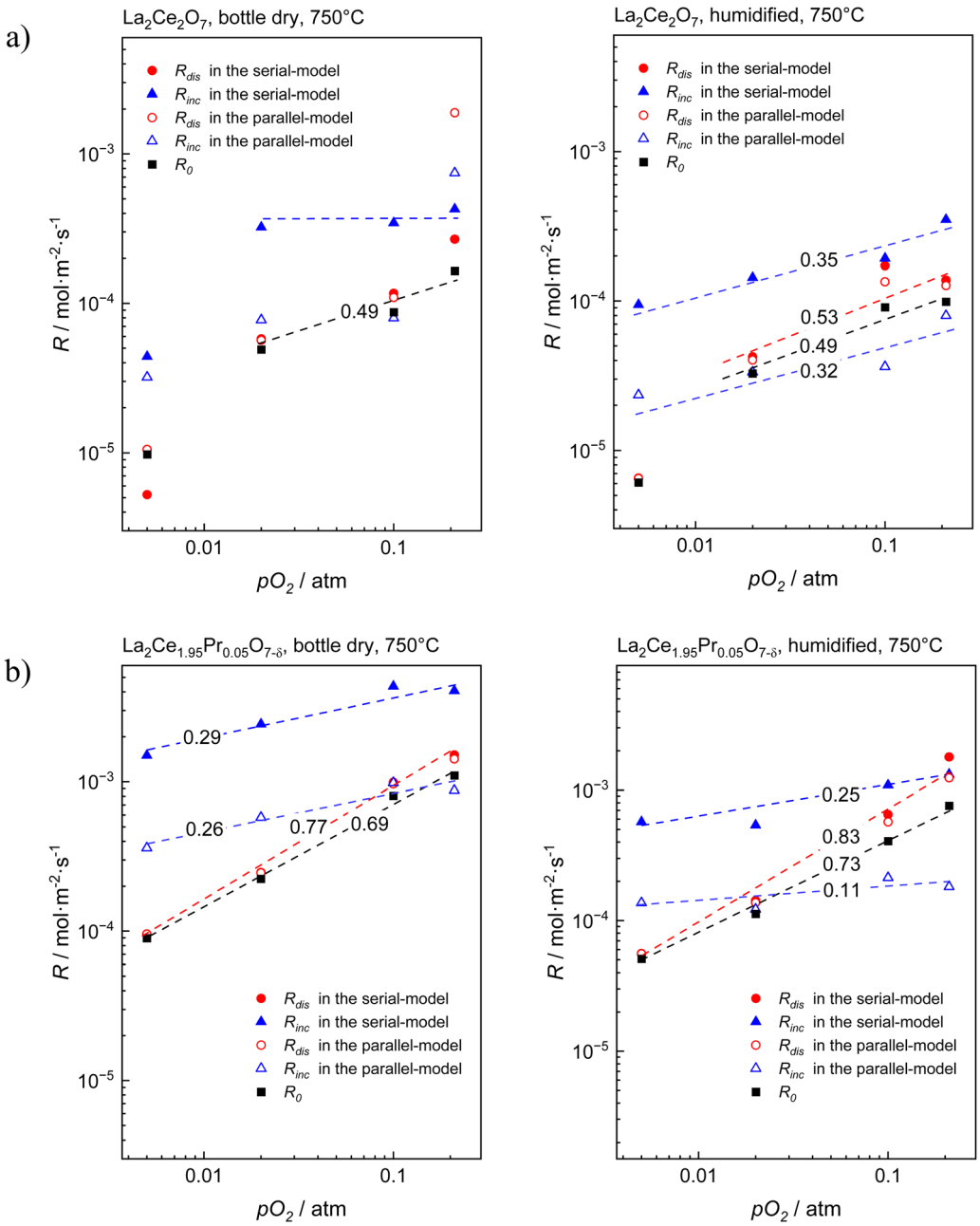

Fig. 8 Oxygen partial pressure dependence of the deconvoluted oxygen surface exchange rates in dry and wet carrier gases for (a) $La_2Ce_2O_7$ and (b) $La_2Ce_{1.95}Pr0_{0.05}O_7$. The entire dataset is presented in the Section S5 (ESI†).

the fact that the La acceptor totally dominates the defect structure of $La_2Ce_2O_7$, we have assumed, as a first approximation, that the p_{O_2} dependence of the concentration of point defects at the surface corresponds to that of the bulk material. It should, however, be recognized that the surfaces of ceria-based materials tend to be more reduced than the bulk.[30]

Previous research has demonstrated that the total electrical conductivity of $La_2Ce_2O_7$ is independent of p_{O_2} under oxidizing conditions, reflecting predominant oxide ion conductivity.[38,39,77–79] This behavior was, as adopted herein, rationalized by considering lanthanum cerate as 50% La-substituted CeO_2. The doping reaction, wherein La^{3+} substitutes for Ce^{4+} and is charge-compensated by formation of oxygen vacancies, can be described as follows:

$$La_2O_3 \xrightarrow{CeO_2} 2La'_{Ce} + v_O^{\bullet\bullet} + 3O_O^{\times} \quad (9)$$

The simplified, limiting electroneutrality (bulk) within the present experimental window is thereby given by:

$$[La'_{Ce}] = 2[v_O^{\bullet\bullet}] \quad (10)$$

The p_{O_2} dependence of the minority electronic defect concentration can be determined from the equilibrium constant of

the redox reactions:

$$O_O^{\times} \rightarrow v_O^{\bullet\bullet} + 2e' + \frac{1}{2}O_2(g) \quad (11)$$

or

$$O_O^{\times} + 2h^{\bullet} \rightarrow v_O^{\bullet\bullet} + \frac{1}{2}O_2(g) \quad (12)$$

Combined with the limiting electroneutrality conditions in eqn (10), the concentrations of electrons and electron holes are accordingly proportional to $p_{O_2}{}^{-1/4}$ and $p_{O_2}{}^{1/4}$, respectively.

Returning to the elementary reactions, rate expressions for the reactions in eqn (2)–(6) can now be derived. Provided that dissociative adsorption is limiting, the elementary reactions in eqn (2), (3) and (6) reach quasi-equilibrium. As PIE represents tracer measurements, the exchange coefficients derived from the isotope profiles reflect the equilibrium exchange rates, $\Re_0$, and can be expressed as:[80]

K_x represents the equilibrium constant for the respective elementary reaction (x denotes the reaction number). The $[\text{species}]_{eq}$ refers to the concentration of the respective species at equilibrium. (Eqn (13)–(16) demonstrate that the p_{O_2} dependence is the same for both the forward and backward reactions, satisfying the principle of microscopic reversibility.)

It is apparent from eqn (13) and (14) that if valence band electrons are involved (leading to the formation of holes) in the rate-determining step, it is not possible to distinguish whether oxygen vacancies participate in the dissociation reaction, as both mechanisms result in $\Re_0 \propto p_{O_2}{}^{3/4}$. This dependence matches relatively well with the observed pressure dependence of $\Re_0$ for the Pr-doped material (*cf.* Fig. 8b), but the deconvoluted experimental data are mostly on the higher side of a 3/4 dependency. There are several possible explanations for the stronger pressure dependence: (i) the defect structure deviates somewhat from that of the bulk, (ii) the first ionization step

$$\Re_{4.a} = \begin{cases} \vec{k}_{4.a}\left[O_{2,ad}^-\right]\left[v_O^{\bullet\bullet}\right] = \vec{k}_{4.a}\left(K_2K_3\dfrac{p_{O_2}}{[h^{\bullet}]}\right)\left[v_O^{\bullet\bullet}\right] \propto p_{O_2}{}^{3/4} & \text{forward reaction} \\ \overleftarrow{k}_{4.a}\left[O_{ad}^-\right]\left[O_O^{\times}\right][h^{\bullet}]^2 = \overleftarrow{k}_{4.a}\left(K_6\dfrac{[O_O^{\times}][h^{\bullet}]}{\left[v_O^{\bullet\bullet}\right]}\right)\left[O_O^{\times}\right][h^{\bullet}]^2 \propto p_{O_2}{}^{3/4} & \text{backward reaction} \end{cases} \quad (13)$$

$$\Re_0^{4.a} = \sqrt{\left(\vec{k}_{4.a}\left[O_{2,ad}^-\right]_{eq}\left[v_O^{\bullet\bullet}\right]_{eq}\right)\left(\overleftarrow{k}_{4.a}\left[O_{ad}^-\right]_{eq}\left[O_O^{\times}\right]_{eq}[h^{\bullet}]_{eq}^2\right)} \propto p_{O_2}{}^{3/4} \quad \text{equilibrium exchange rate}$$

$$\Re_{4.b} = \begin{cases} \vec{k}_{4.b}\left[O_{2,ad}^-\right] = \vec{k}_{4.b}\left(K_2K_3\dfrac{p_{O_2}}{[h^{\bullet}]}\right) \propto p_{O_2}{}^{3/4} & \text{forward reaction} \\ \overleftarrow{k}_{4.b}\left[O_{ad}^-\right]^2[h^{\bullet}] = \overleftarrow{k}_{4.b}\left(K_6\dfrac{[O_O^{\times}][h^{\bullet}]}{\left[v_O^{\bullet\bullet}\right]}\right)^2[h^{\bullet}] \propto p_{O_2}{}^{3/4} & \text{backward reaction} \end{cases} \quad (14)$$

$$\Re_0^{4.b} = \sqrt{\left(\vec{k}_{4.b}\left[O_{2,ad}^-\right]_{eq}\right)\left(\overleftarrow{k}_{4.b}\left[O_{ad}^-\right]_{eq}^2[h^{\bullet}]_{eq}\right)} \propto p_{O_2}{}^{3/4} \quad \text{equilibrium exchange rate}$$

when electron holes are involved in the rate-determining step according to eqn (4). If instead electrons are at play, the effects of varying the oxygen partial pressure would correspond to:

$$\Re_{5.a} = \begin{cases} \vec{k}_{5.a}\left[O_{2,ad}^-\right][e']^2\left[v_O^{\bullet\bullet}\right] = \vec{k}_{5.a}\left(K_2K_3\dfrac{p_{O_2}}{[h^{\bullet}]}\right)[e']^2\left[v_O^{\bullet\bullet}\right] \propto p_{O_2}{}^{1/4} & \text{forward reaction} \\ \overleftarrow{k}_{5.a}\left[O_{ad}^-\right]\left[O_O^{\times}\right] = \overleftarrow{k}_{5.a}\left(K_6\dfrac{[O_O^{\times}][h^{\bullet}]}{\left[v_O^{\bullet\bullet}\right]}\right)\left[O_O^{\times}\right] \propto p_{O_2}{}^{1/4} & \text{backward reaction} \end{cases} \quad (15)$$

$$\Re_0^{5.a} = \sqrt{\left(\vec{k}_{5.a}\left[O_{2,ad}^-\right]_{eq}[e']_{eq}^2\left[v_O^{\bullet\bullet}\right]_{eq}\right)\left(\overleftarrow{k}_{5.a}\left[O_{ad}^-\right]_{eq}\left[O_O^{\times}\right]_{eq}\right)} \propto p_{O_2}{}^{1/4} \quad \text{equilibrium exchange rate}$$

$$\Re_{5.b} = \begin{cases} \vec{k}_{5.b}\left[O_{2,ad}^-\right][e'] = \vec{k}_{5.b}\left(K_2K_3\dfrac{p_{O_2}}{[h^{\bullet}]}\right)[e'] \propto p_{O_2}{}^{1/2} & \text{forward reaction} \\ \overleftarrow{k}_{5.b}\left[O_{ad}^-\right]^2 = \overleftarrow{k}_{5.b}\left(K_6\dfrac{[O_O^{\times}][h^{\bullet}]}{\left[v_O^{\bullet\bullet}\right]}\right)^2 \propto p_{O_2}{}^{1/2} & \text{backward reaction} \end{cases} \quad (16)$$

$$\Re_0^{5.b} = \sqrt{\left(\vec{k}_{5.b}\left[O_{2,ad}^-\right]_{eq}[e']_{eq}\right)\left(\overleftarrow{k}_{5.b}\left[\left[O_{ad}^-\right]_{eq}^2\right]\right)} \propto p_{O_2}{}^{1/2} \quad \text{equilibrium exchange rate}$$

may be partly constrained, and (iii) if the adsorption and dissociation occur directly at the oxygen vacancy, with the transfer of three electronic species, bypassing the initial adsorption step. Nonetheless, it will be evident later that the influence of humidity points toward the contribution of oxygen vacancies in the rate-determining step.

If instead conduction band electrons are involved in the rate-determining step, eqn (15) and (16) show that different pressure dependences emerge for the parallel-like and serial dissociation mechanisms. For the LaC data, $\Re_{dis}$ is proportional to $p_{O_2}{}^{\sim 1/2}$ (*cf.* Fig. 8a), which corresponds to the dependence expected for the serial mechanism where conduction band electrons are the ionization source of the oxygen species (eqn (16)). Overall, evaluation of the oxygen partial pressure dependences indicates that pristine LaC follows the serial mechanism with conduction band electrons ionizing the oxygen species, whereas for the Pr-doped material, valence band electrons predominate.

Deviating effects of water vapor on oxygen exchange kinetics have been reported in the literature.[81–86] In this respect, it is important to recognize the conceptual differences in the exchange of oxygen between surface oxide ions and (i) the oxide ion in water, and (ii) the oxygen molecules. The former represents an acid–base reaction involving no net transfer of electronic species, while the latter, overall, is a redox reaction. We will now attempt to gain further insight to the exchange mechanism through the effects of humidity on the data.

Since water vapor decreases the oxygen exchange rate and increases the apparent activation energy without significantly changing the dependence on oxygen partial pressure, we infer that hydroxide groups adsorb onto oxygen vacancies, partly blocking the adsorption of oxygen (eqn (4-a) and (5-a)). $La_2Ce_2O_7$ favorably dissolves hydroxide defects *via* dissociative adsorption of water into oxygen vacancies,[39,44] and the surface of the lanthanum cerate is relatively basic, generally promoting hydration.[87] On these bases, we presume that hydroxide groups are relatively strongly bonded to oxygen vacancies during annealing in wet carrier gas and, at least partly, remain adsorbed during the $^{36}O_2$ pulse, although it is dry. Since hydration of surface oxygen vacancies is exothermic, the concentration of hydroxide defects at the surface decreases with increasing temperature, gradually reducing the effect of humidity on the exchange rate. This is consistent with the diminishing difference between the dry and wet datasets as the temperature rises (*cf.* Fig. 5), supporting the rationale behind the water effect.

A close evaluation of the effects of humidified conditions reveals that the activation energy of $\Re_{dis}$ for LaC is independent of the level of humidification. In contrast, the activation energy increases for $\Re_{inc}$ for LaC, similarly also for both $\Re_{dis}$ and $\Re_{inc}$ for 5PrLaC (see Fig. 4). Since dissociative adsorption according to the serial mechanism (eqn (4-b) and (5-b)) is the only elementary reaction not involving oxygen vacancies, these findings again support the hypothesis that hydroxide groups block oxygen vacancies. Further, it indirectly supports that the pristine and Pr-substituted $La_2Ce_2O_7$ follow different exchange mechanisms. Finally, the fact that both $\Re_{dis}$ and $\Re_{inc}$ for 5PrLaC exhibit higher apparent activation energies under humidified compared to bottle-dry conditions, shows that the oxygen exchange for the doped material is facilitated by oxygen vacancies and follows the parallel-like mechanism.

In interpreting the oxygen partial pressure dependence of the faster elementary steps, the reactions are at equilibrium and depend on the concentration of the defects taking part. If we assume that electron holes enter the incorporation step (eqn (6)), then the corresponding reaction rate follows a $p_{O_2}{}^{1/4}$ dependence; otherwise, if electrons do, the reaction rate will be independent of p_{O_2}. Despite scattering, the behaviour of the incorporation data generally reflects this trend (*cf.* Fig. 8).

So far, we have not directly addressed the effects of Pr substitution, *i.e.*, the overall slightly increased exchange rates and the apparent activation energy decreasing from $\sim$150 kJ mol^{-1} to $\sim$120 kJ mol^{-1} under dry conditions. Presumably, the bond strength between Pr(III) and oxygen is weaker than for the Ce(IV)-oxygen bond, which would promote the oxygen exchange compared to LaC. Moreover, the addition of Pr(III) will increase the level of acceptor dopants and, consequently, the concentration of oxygen vacancies. However, given the low concentration of Pr, relative to the inherently high oxygen vacancy concentration in lanthanum cerates, we believe that this minute change in composition does not affect the vacancy concentration sufficiently, nor the potential effect of weaker metal–oxygen bonds, enough to account for the changes in $\Re_0$. Therefore, it is plausible to suggest that the effects of Pr doping are related to its multiple valence states. Similar effects of Pr on the oxygen exchange rate have been observed for other rare-earth substituted ceria materials, scaling with the concentration of Pr.[21] The nominal Pr concentration in the present study is below the reported threshold where the formation of continuous Pr impurity bands are suggested to form within the CeO_2 bandgap.[27,28,88] Nevertheless, the electronic conductivity has been shown to increase significantly for ceria-based materials, even with Pr levels below 5%, indicating that even low Pr concentrations affect the level of electronic defects in ceria-based materials.[21] Moreover, Schaube *et al.*,[21] reported an enrichment of Pr at the surface relative to nominal bulk values for Pr-substituted CeO_2. Provided that 5PrLaC behaves similarly, we speculate that the Pr concentration at the surface reaches levels where its multiple oxidation states will affect the surface electronic states, to some extent enhancing the overlap with the electronic states of the adsorbate. Overall, this would increase the oxygen exchange rate and decrease its activation energy.[26–28]

According to the differences in the behaviour of the two materials, the electronic defect responsible for the ionization of the adsorbed oxygen species, indeed, changes from conduction band electrons for pristine lanthanum cerate to valence band electrons for the Pr-doped version. Whether valence band or conduction band electrons ionize the adsorbed oxygen species depends on the overlap between electron band structure of the surface and that of adsorbed oxygen species – more specifically, the position of the adsorbate energy level relative to the conduction and valence band for the surface cations, and, not least, the Fermi level. Thereby, the encountered change in the

oxygen exchange mechanism between the two materials may support that the Pr concentration on the surface is enriched compared to the nominal values and sufficient to alter the electronic properties at the surface.

As pointed out earlier, the effect of water on the apparent activation energy is stronger for the Pr-doped material compared to the pristine LaC (*cf.* Fig. 5). Presumably, this is also related to the Pr^{3+}/Pr^{4+} couple, and one may speculate whether this effect relates to the balance between hydration and hydrogenation at the surface.

Finally, one should compare the results from the present study with relevant literature. There is significant scatter in the literature data when comparing rates and activation energies of oxygen exchange kinetics; even for identical compositions, exchange rates may vary by orders of magnitude.[21] Despite this, it is still useful to compare lanthanum cerates to relevant literature on rare-earth-substituted ceria. Nicollet *et al.*[50] reported that the activation energy increases with increasing concentration of La, with values in the range of 1 eV for $La_{0.1}(Ce_{0.9}Pr_{0.1})_{0.9}O_{2-\delta}$. This is generally lower than the activation energy determined here for the lanthanum cerates, and the present data consequently supports the claim of Nicollet *et al.*[50] Comparing the data from Schaube *et al.*[21] to the current study for similar compositions and conditions, the oxygen exchange rates and activation energies are in the same ballpark.

6. Conclusion

The oxygen surface exchange mechanism for $La_2Ce_2O_7$ and $La_2Ce_{1.95}Pr_{0.05}O_{7-\delta}$ has been investigated using the pulse isotope exchange technique. The exchange is rate-limited by oxygen vacancy-mediated dissociation of adsorbed oxygen species.

Water vapor decreases the oxygen exchange rate and increases its apparent activation energy. This behavior reflects preferential, exothermic dissociative adsorption of water, blocking surface oxygen vacancies.

The activation energy is lower, and the exchange rate is higher for 5 mol% Pr-doped $La_2Ce_2O_7$ compared to that of nominal $La_2Ce_2O_7$, implying that electronic species introduced by the redox-active Pr ions facilitate the transfer of electronic species during the exchange process.

The effect of water on oxygen exchange is more prominent for 5 mol% Pr-doped $La_2Ce_2O_7$, indicating that the hydrogenation mediated by the Pr^{3+}/Pr^{4+} couple at the surface affects the charge transfer process.

Author contributions

Yizhou Shen: writing – original draft, conceptualization, investigation, formal analysis, visualization. Vincent Thoréton: review & editing, supervision. Reidar Haugsrud: writing – review & editing, conceptualization, supervision.

Data availability

The authors confirm that the data supporting the findings of this study are available within the article and its ESI.†

Conflicts of interest

The authors declare that they have no known competing financial interests or personal relationships that could have influenced the work reported in this paper.

Acknowledgements

The authors acknowledge the support of the FRINATEK project 262393 ''Fundamentals of Surface Kinetics in High Temperature Electrochemistry'' (FUSKE) of the Research Council of Norway.

References

1 Z. Shao and S. M. Haile, *Materials for Sustainable Energy: A Collection of Peer-Reviewed Research and Review Articles from Nature Publishing Group*, 2010, vol. 3, pp. 255–258.
2 N. Mahato, A. Banerjee, A. Gupta, S. Omar and K. Balani, *Prog. Mater. Sci.*, 2015, **72**, 141–337.
3 Q. Xu, Z. Guo, L. Xia, Q. He, Z. Li, I. Temitope Bello, K. Zheng and M. Ni, *Energy Convers. Manag.*, 2022, **253**, 115175.
4 E. P. Murray, T. Tsai and S. A. Barnett, *Nature*, 1999, **400**, 649–651.
5 W. C. Chueh, A. H. McDaniel, M. E. Grass, Y. Hao, N. Jabeen, Z. Liu, S. M. Haile, K. F. McCarty, H. Bluhm and F. El Gabaly, *Chem. Mater.*, 2012, **24**, 1876–1882.
6 R. Schmitt, A. Nenning, O. Kraynis, R. Korobko, A. I. Frenkel, I. Lubomirsky, S. M. Haile and J. L. M. Rupp, *Chem. Soc. Rev.*, 2020, **49**, 554–592.
7 H. Inaba and H. Tagawa, *Solid State Ionics*, 1996, **83**, 1–16.
8 C. Sánchez-Bautista, A. J. Dos Santos-García, J. Peña-Martínez and J. Canales-Vázquez, *Solid State Ionics*, 2010, **181**, 1665–1673.
9 B. Matović, M. Stojmenović, J. Pantić, A. Varela, M. Žunić, N. Jiraborvornpongsa and T. Yano, *J. Asian Ceram. Soc.*, 2014, **2**, 117–122.
10 P. Shuk and M. Greenblatt, *Solid State Ionics*, 1999, **116**, 217–223.
11 L. Li, G. Li, Y. Che and W. Su, *Chem. Mater.*, 2000, **12**, 2567–2574.
12 M. A. Małecka, L. Kepiński and M. Maczka, *J. Solid State Chem.*, 2008, **181**, 2306–2312.
13 W. Miśta, M. A. Małecka and L. Kepiński, *Appl. Catal., A*, 2009, **368**, 71–78.
14 V. Grover, A. Banerji, P. Sengupta and A. K. Tyagi, *J. Solid State Chem.*, 2008, **181**, 1930–1935.
15 B. Zachau-Christiansen, *ECS Proc. Vol.*, 1993, **1993–4**, 104–111.

16 M. Melchionna and P. Fornasiero, *Mater. Today*, 2014, **17**, 349–357.
17 T. Montini, M. Melchionna, M. Monai and P. Fornasiero, *Chem. Rev.*, 2016, **116**, 5987–6041.
18 M. Mogensen, N. M. Sammes and G. A. Tompsett, *Solid State Ionics*, 2000, **129**, 63–94.
19 V. V. Kharton, F. M. Figueiredo, L. Navarro, E. N. Naumovich, A. V. Kovalevsky, A. A. Yaremchenko, A. P. Viskup, A. Carneiro, F. M. B. Marques and J. R. Frade, *J. Mater. Sci.*, 2001, **36**, 1105–1117.
20 A. Bueno-López, K. Krishna, M. Makkee and J. A. Moulijn, *J. Catal.*, 2005, **230**, 237–248.
21 M. Schaube, R. Merkle and J. Maier, *J. Mater. Chem. A*, 2019, **7**, 21854–21866.
22 L. Li, X. Lin, G. Li and H. Inomata, *J. Mater. Res.*, 2001, **16**, 3207–3213.
23 E. Ruiz-Trejo, J. D. Sirman, Y. M. Baikov and J. A. Kilner, *Solid State Ionics*, 1998, **113–115**, 565–569.
24 Z. Zhan, T.-L. Wen, H. Tu and Z.-Y. Lu, *J. Electrochem. Soc.*, 2001, **148**, A427.
25 S. A. Acharya, *J. Power Sources*, 2012, **198**, 105–111.
26 J. J. Kim, S. R. Bishop, D. Chen and H. L. Tuller, *Chem. Mater.*, 2017, **29**, 1999–2007.
27 S. R. Bishop, T. S. Stefanik and H. L. Tuller, *Phys. Chem. Chem. Phys.*, 2011, **13**, 10165–10173.
28 S. R. Bishop, T. S. Stefanik and H. L. Tuller, *J. Mater. Res.*, 2012, **27**, 2009–2016.
29 D. Chen, S. R. Bishop and H. L. Tuller, *J. Electroceram.*, 2012, **28**, 62–69.
30 Q. Lu, G. Vardar, M. Jansen, S. R. Bishop, I. Waluyo, H. L. Tuller and B. Yildiz, *Chem. Mater.*, 2018, **30**, 2600–2606.
31 P. S. Manning, J. D. Sirman and J. A. Kilner, *Solid State Ionics*, 1996, **93**, 125–132.
32 K. Kowalski, *Defect Diffus. Forum*, 2009, **289–292**, 769–774.
33 S. P. Waldow, B. J. Statham, H. F. Wardenga, T. E. Weirich, A. Klein and R. A. De Souza, *ACS Appl. Mater. Interfaces*, 2020, **12**, 36768–36777.
34 E. Reynolds, P. E. R. Blanchard, Q. Zhou, B. J. Kennedy, Z. Zhang and L. Y. Jang, *Phys. Rev. B: Condens. Matter Mater. Phys.*, 2012, **85**(13), 132101.
35 L. E. Kalland, S. T. Norberg, J. Kyrklund, S. Hull, S. G. Eriksson, T. Norby, C. E. Mohn and C. S. Knee, *Phys. Chem. Chem. Phys.*, 2016, **18**, 24070–24080.
36 H. Yamamura, H. Nishino, K. Kakinuma and K. Nomura, *J. Ceram. Soc. Jpn.*, 2003, **111**(1300), 902–906.
37 F. J. Trindade, S. Damasceno, L. Otubo, M. R. Felez, D. Z. De Florio, F. C. Fonseca and A. S. Ferlauto, *ACS Appl. Nano Mater.*, 2022, **5**, 8859–8867.
38 S. A. Ismail, L. Jiang, P. Zhong, T. Norby and D. Han, *J. Alloys Compd.*, 2022, **899**, 163306.
39 V. Besikiotis, C. S. Knee, I. Ahmed, R. Haugsrud and T. Norby, *Solid State Ionics*, 2012, **228**, 1–7.
40 B. C. H. Steele and A. Heinzel, *Nature*, 2001, **414**, 345–352.
41 L. Yan, W. Sun, L. Bi, S. Fang, Z. Tao and W. Liu, *Int. J. Hydrogen Energy*, 2010, **35**, 4508–4511.
42 W. Sun, S. Fang, L. Yan and W. Liu, *Fuel Cells*, 2012, **12**, 457–463.
43 Z. Zhu, B. Liu, J. Shen, Y. Lou and Y. Ji, *J. Alloys Compd.*, 2016, **659**, 232–239.
44 L. E. Kalland, A. Løken, T. S. Bjørheim, R. Haugsrud and T. Norby, *Solid State Ionics*, 2020, **354**, 115401.
45 Y. Ling, J. Chen, Z. Wang, C. Xia, R. Peng and Y. Lu, *Int. J. Hydrogen Energy*, 2013, **38**, 7430–7437.
46 J. De Wang, Y. H. Xie, Z. F. Zhang, R. Q. Liu and Z. J. Li, *Mater. Res. Bull.*, 2005, **40**, 1294–1302.
47 Y. Zhang, J. Xu, X. Xu, R. Xi, Y. Liu, X. Fang and X. Wang, *Catal. Today*, 2020, **355**, 518–528.
48 C. Madhuri, K. Venkataramana, A. Nurhayati and C. V. Reddy, *Curr. Appl. Phys.*, 2018, **18**, 1134–1142.
49 A. Kalpana Devi, G. Ram Kumar, C. Prerna, K. Amarsingh Bhabu, V. Sabarinathan and T. R. Rajasekaran, *J. Mater. Sci.: Mater. Electron.*, 2020, **31**, 10628–10638.
50 C. Nicollet, D. Kalaev and H. L. Tuller, *Solid State Ionics*, 2019, **331**, 96–101.
51 W. C. Jung and H. L. Tuller, *Adv. Energy Mater.*, 2011, **1**, 1184–1191.
52 J. A. Kilner, *Solid State Ionics*, 2000, **129**, 13–23.
53 F. A. Kröger and H. J. Vink, *Solid State Phys. – Adv. Res. Appl.*, 1956, **3**, 307–435.
54 C. B. Gopal and S. M. Haile, *J. Mater. Chem. A*, 2014, **2**, 2405–2417.
55 Z. Li, T. Norby and R. Haugsrud, *J. Am. Ceram. Soc.*, 2012, **95**, 2065–2073.
56 J. A. Kilner, B. C. H. Steele and L. Ilkov, *Solid State Ionics*, 1984, **12**, 89–97.
57 R. J. Chater, S. Carter, J. A. Kilner and B. C. H. Steele, *Solid State Ionics*, 1992, **53–56**, 859–867.
58 M. V. Ananyev, E. S. Tropin, V. A. Eremin, A. S. Farlenkov, A. S. Smirnov, A. A. Kolchugin, N. M. Porotnikova, A. V. Khodimchuk, A. V. Berenov and E. K. Kurumchin, *Phys. Chem. Chem. Phys.*, 2016, **18**, 9102–9111.
59 Z. Li, R. Haugsrud and T. Norby, *Solid State Ionics*, 2011, **184**, 42–46.
60 H. J. M. Bouwmeester, C. Song, J. Zhu, J. Yi, M. Van Sint Annaland and B. A. Boukamp, *Phys. Chem. Chem. Phys.*, 2009, **11**, 9640–9643.
61 C. Y. Yoo and H. J. M. Bouwmeester, *Phys. Chem. Chem. Phys.*, 2012, **14**, 11759–11765.
62 C. L. Song, J. X. Yi and Y. Yan, *Chinese J. Chem. Phys.*, 2019, **32**, 474–484.
63 R. Merkle and J. Maier, *Phys. Chem. Chem. Phys.*, 2002, **4**, 4140–4148.
64 R. A. De Souza, *Phys. Chem. Chem. Phys.*, 2006, **8**, 890–897.
65 Y. M. Choi, H. Abernathy, H. T. Chen, M. C. Lin and M. Liu, *Chem. Phys. Chem.*, 2006, **7**, 1957–1963.
66 C. Yang, X. Yu, S. Heißler, P. G. Weidler, A. Nefedov, Y. Wang, C. Wöll, T. Kropp, J. Paier and J. Sauer, *Angew. Chem., Int. Ed.*, 2017, **56**, 16399–16404.
67 Z. Wu, M. Li, J. Howe, H. M. Meyer and S. H. Overbury, *Langmuir*, 2010, **26**, 16595–16606.
68 R. Merkle, M. F. Hoedl, G. Raimondi, R. Zohourian and J. Maier, *Annu. Rev. Mater. Res.*, 2021, **51**, 461–493.

69 L. Wang, R. Merkle, Y. A. Mastrikov, E. A. Kotomin and J. Maier, *J. Mater. Res.*, 2012, **27**, 2000–2008.
70 M. M. Kuklja, E. A. Kotomin, R. Merkle, Y. A. Mastrikov and J. Maier, *Phys. Chem. Chem. Phys.*, 2013, **15**, 5443–5471.
71 Z. Guan, D. Chen and W. C. Chueh, *Phys. Chem. Chem. Phys.*, 2017, **19**, 23414–23424.
72 M. W. Den Otter, B. A. Boukamp and H. J. M. Bouwmeester, *Solid State Ionics*, 2001, **139**, 89–94.
73 H. J. M. B. and A. J. B. B. A. Boukamp, in Proceedings of the Second International Symposium on Ionic and Mixed Conducting Ceramics, ed. W. L. W. and H. L. T. T. A. Ramanarayanan, The Electrochemical Society, 1994, p. 141.
74 K. Klier, J. Novakova and P. Jiru, *J. Catal.*, 1963, **484**, 479–484.
75 G. K. Boreskov and V. S. Muzykantov, *Ann. N. Y. Acad. Sci.*, 1973, **213**, 137–170.
76 D. Poetzsch, R. Merkle and J. Maier, *Adv. Funct. Mater.*, 2015, **25**, 1542–1557.
77 E. Suda, B. Pacaud and M. Mori, *J. Alloys Compd.*, 2006, **408–412**, 1161–1164.
78 H. Tinwala, P. Shah, K. Siddhapara, D. Shah and J. Menghani, *J. Cryst. Growth*, 2016, **452**, 54–56.
79 K. Sandhya, N. S. Chitrapriya, P. K. Aswathy and D. N. Rajendran, *Mater. Today: Proc.*, 2019, **10**, 112–120.
80 J. Maier, *Solid State Ionics*, 1998, **112**, 197–228.
81 R. A. De Souza, *J. Mater. Chem. A*, 2017, **5**, 20334–20350.
82 S. J. Cooper, M. Niania, F. Hoffmann and J. A. Kilner, *Phys. Chem. Chem. Phys.*, 2017, **19**, 12199–12205.
83 M. J. Pietrowski, R. A. De Souza, M. Fartmann, R. Ter Veen and M. Martin, *Fuel Cells*, 2013, **13**, 673–681.
84 M. Molinari, S. C. Parker, D. C. Sayle and M. S. Islam, *J. Phys. Chem. C*, 2012, **116**, 7073–7082.
85 N. Sakai, K. Yamaji, T. Horita, H. Kishimoto, Y. P. Xiong and H. Yokokawa, *Phys. Chem. Chem. Phys.*, 2003, **5**, 2253–2256.
86 N. Sakai, K. Yamaji, T. Horita, Y. P. Xiong, H. Kishimoto and H. Yokokawa, *J. Electrochem. Soc.*, 2003, **150**, A689.
87 T. Norby, M. Widerøe, R. Glöckner and Y. Larring, *Dalton Trans.*, 2004, 3012–3018.
88 H. L. Tuller and A. S. Nowick, *J. Phys. Chem. Solids*, 1977, **38**, 859–867.